Available online at www.sciencedirect.com
ScienceDirect
Journal of the European Ceramic Society 30 (2010) 1649–1657
www.elsevier.com/locate/jeurceramsoc

Thermal cycling behaviors of the plasma sprayed thermal barrier coatings of hexaluminates with magnetoplumbite structure

Xiaolong Chen [a,b], Yanfei Zhang [a,b], Xinhua Zhong [a,b], Zhenhua Xu [a,b], Jiangfeng Zhang [a,b], Yongliang Cheng [a,b], Yu Zhao [a,b], Yangjia Liu [c], Xizhi Fan [c], Ying Wang [a], Hongmei Ma [a], Xueqiang Cao [a,*]

[a] *State Key Laboratory of Rare Earth Resources Utilization, Changchun Institute of Applied Chemistry, Chinese Academy of Sciences, Changchun 130022, China*
[b] *Graduate School of the Chinese Academy of Sciences, Beijing 100049, China*
[c] *Hunan Provincial Key Laboratory of Materials Protection for Electric Power and Transportation, Changsha University of Science & Technology, Changsha 410004, China*

Received 31 July 2009; received in revised form 28 December 2009; accepted 10 January 2010
Available online 2 February 2010

Abstract

Hexaluminates with magnetoplumbite structure are important high temperature ceramic materials for thermal barrier coatings (TBCs). Four hexaluminate coatings including $NdMgAl_{11}O_{19}$ (NdMA), $SmMgAl_{11}O_{19}$ (SmMA), $GdMgAl_{11}O_{19}$ (GdMA) and $SrAl_{12}O_{19}$ (SrHA) were prepared by plasma spraying. During plasma spraying, rare earth (RE) hexaluminates are partially decomposed, resulting in the loss of MgO. For RE hexaluminate coatings, the thermal cycling lifetime decreases with the reduction of RE^{3+} radius, while SrHA has the shortest lifetime. The random arrangement of the platelet-like hexagonal crystals resulted from the recrystallization during thermal cycling may reduce the bond strength of the coatings and make a large contribution to coatings' failure. The different thermal cycling behaviors of these coatings seem to be dependent on their recrystallization differences to a large extent.

Keywords: Thermal barrier coatings; Magnetoplumbite; Plasma spraying; Thermal cycling behavior

1. Introduction

Ceramic coatings are widely served as thermal, wear and corrosion barriers in modern industries. Wherein, thermal barrier coatings (TBCs) are playing an important role in the development of the next generation aerospace gas-turbine engines. TBCs provide thermal protection to the superalloy blades and enable engines to be operated at higher gas inlet temperature, giving rise to the improvements of the thrust-to-weight ratio, lifetime and fuel efficiency of the aerospace engines. Currently, a TBC system consists of two layers, including a superalloy bond coat (MCrAlY, M = Ni, Co) as the oxidation resistant layer and a ceramic top-coat as the heat resistant layer. The mismatch of thermal and mechanical properties between the bond coat and ceramic coating is the key factor to determine the performance of TBCs. The moderate coefficient of thermal expansion (CTE) compared to that of bond coat ($\sim 14 \times 10^{-6}\,K^{-1}$)[1] and low thermal conductivity are the first two selection criteria of TBC candidate materials. Nowadays, plasma spraying (PS) and electron-beam physical vapor deposition (EB-PVD) are the two main methods for the fabrication of TBCs. 6–8 wt% yttria stabilized zirconia (YSZ) is the state-of-the-art ceramic top-coat TBC material. However, previous studies indicate that phase transformation, sintering in combination with the increase of Young's modulus of YSZ coating limit its application temperature below 1200 °C.[1–9]

During last decades, much efforts have been devoted to develop new alternative TBC materials to YSZ for applications above 1200 °C. Zirconates with pyrochlore-type structure ($RE_2Zr_2O_7$, RE = La, Pr, Nd, Sm, Eu, Gd) and perovskite-type structure ($BaZrO_3$, $SrZrO_3$),[10–13] rare earth composite oxides with fluorite-type structure ($La_2Ce_2O_7$, $Nd_2Ce_2O_7$)[14,15] have been proposed as new TBC candidate materials. However, the relative low CTEs of pyrochlore-type oxides and the poor high

* Corresponding author. Tel.: +86 431 85262285; fax: +86 431 85262285.
E-mail address: xcao@ciac.jl.cn (X. Cao).

0955-2219/$ – see front matter © 2010 Elsevier Ltd. All rights reserved.
doi:10.1016/j.jeurceramsoc.2010.01.013

temperature phase stability of perovskite-type zirconates impart the thermal cycling properties of these coatings inferior to that of YSZ coating.[6]

Recently, a large class of hexaluminates with magnetoplumbite structure whose chemical composition is $LnMeAl_{11}O_{19}$ (Ln = La, Pr, Nd, Sm, Eu, Gd, Ca, Sr; Me = Mg, Mn, Fe, Co, Ni, Cu, Zn) have been proposed as new TBC materials.[16,17] Actually, the research about $LnMeAl_{11}O_{19}$ as laser and luminescent materials and high temperature combustion catalysts can be dated back to 1980s. These oxides have the platelet-like hexagonal grains with high aspect ratio, and they can be used as the reinforce phases in ceramic matrix composites.[18–22] Such oxides have good thermochemical stability up to 1400 °C, making them the promising materials for high temperature applications. The thermal physical properties of lanthanum magnesium hexaluminate (LaMA) and its coating preparation have been studied by Gadow et al.[23–26] The thermal properties of the bulk materials of some RE hexaluminates have also been reported by Bansal.[16,17] In our former work, the failure of LaMA coating and the thermal shock resistance of $REMgAl_{11}O_{19}$ (RE = La, Nd, Sm, Gd) bulk materials were studied.[27,28] As a continuing work, coatings of $REMgAl_{11}O_{19}$ (RE = Nd, Sm, Gd) and $SrAl_{12}O_{19}$ with magnetoplumbite structure are prepared by plasma spraying and their thermal cycling behaviors are investigated in the present study.

2. Experimental

Four different ceramic powders of NdMA, SmMA, GdMA and SrHA were synthesized by solid state reaction. Rare earth oxides of Nd_2O_3, Sm_2O_3 and Gd_2O_3 (99.99%) were mixed with MgO (99.2%) and γ-Al_2O_3 (99.99%) in stoichiometric ratio, respectively. $SrCO_3$ (99.0%) and γ-Al_2O_3 were selected as the starting materials for the synthesis of SrHA. Synthesis of these hexaluminates were carried out at 1650 °C for 24 h, and this process was repeated for three times to obtain pure products. The as-synthesized ceramic powders were spray-dried, and the powders with particle size of 20–100 μm were directly used for plasma spraying.

The four different hexaluminate coatings were prepared by atmospheric plasma spraying using a Praxair-Tafa 5500-2000 Plasma Spray unit with a SG-100 gun. These coatings (~330 μm in thickness) were deposited with the same optimized parameters as listed in Table 1. Both the disk-shaped Ni-based superalloy and stainless-steel substrates (diameter = 30 mm, thickness = 3 mm) were simultaneously deposited for each coating material. The superalloy substrates with a MCrAlY (M = Ni, Co, Fe) bond coat about 200 μm in thickness were deposited for burner-rig tests with a coal gas flame, and the coating on stainless-steel substrates were used for the characterization of spraying conditions. The thermal cycling test of the coating was finished by heating the coating surface from room temperature to 1250 ± 30 °C for 5 min followed by quenching for 2 min by a compressed air jet, while the substrate temperatures was at 970 ± 15 °C during heating. This process was repeated until a clearly visible coating surface area of 5% was lost. Infrared-radiation pyrometer (λ = 9.6–11.5 μm) was used to monitor the surface temperature of the coating, and the substrate temperature was measured by a standard Pt/Pt-Rh_{10} thermal couple.

The microstructures of the coatings were characterized using a scanning electron microscope (SEM, XL-30 ESEM FEG, Micro FEI Philips) equipped with an energy dispersive X-ray spectroscopy (EDS). All the coatings for SEM cross-section analysis were embedded in a transparent epoxy resin and polished with diamond pastes, while the surface and fractured cross-section were directly analyzed without other treatments. The phase analysis of coatings before and after thermal cycling were carried out by X-ray diffraction (XRD, Bruker D8 Advance diffractometer, Cu-K_α radiation, λ = 0.15406 nm).

3. Results and discussion

3.1. Thermal cycling tests

The state-of-the-art YSZ coating can be successfully deposited by EB-PVD since Y_2O_3 and ZrO_2 have similar vapor pressures. However, it is difficult to produce the MgO-doped RE hexaluminate coatings by EB-PVD. The extremely high vapor pressure of MgO leads to a serious stoichiometry deviation during the EB-PVD process,[29] resulting in a poor quality coating. Plasma spraying is an ideal process for the preparation of such coatings. Fig. 1 shows a representative microstructure of the plasma sprayed NdMA coating. As illustrated in Fig. 1(a), the cross-section micrograph of the as-sprayed coating indicates that the ceramic powder has a good melting condition during plasma spraying and the adhesion of the coating to the bond coat is perfect. The fine pores (size <0.3 μm) as observed in Fig. 1(a) can be attributed to the incomplete contact between lamellae and the microcracks arising from thermal stresses, and large pores to "holes" are induced by imperfect layer building-up by the melt droplets during plasma spraying. Plasma spraying is a complex thermo-dynamic transformation process. Ceramic powders with certain size distribution were melted and accelerated by the plasma flame, followed by rapidly impacting onto the substrate to form the lamellae structure. Fig. 1(b) shows the surface microstructure of the as-sprayed coating. It has a rough surface

Table 1
Plasma spraying parameters for the four magnetoplumbite oxide coatings deposition.

Spray distance (mm)	Voltage (V)	Current (A)	Plasma gas, standard liter per minute (slpm)	Carrier gas, Ar (slpm)	Powder feed ($g\,min^{-1}$)
120	65	626	Ar: 35.1 H_2: 10.1	3	30

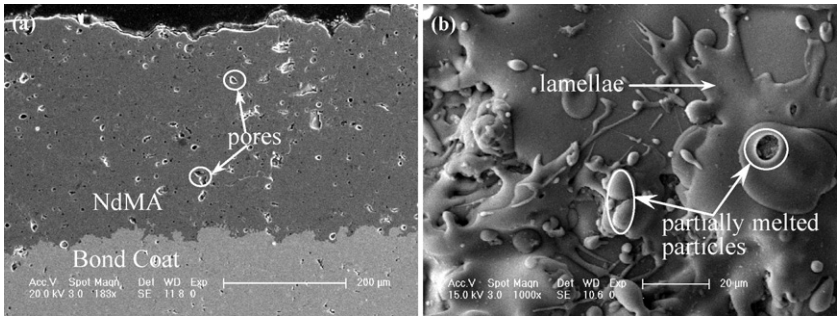

Fig. 1. SEM micrographs of as-sprayed NdMA coating: (a) cross-section and (b) surface.

with some partially melted ceramic powders, the lamellae and some open surface pores could also be observed. The quenching of the molten ceramic particles from the plasma flame to the substrate whose temperature is about 200–300 °C usually produces metastable phases. After plasma spraying, these four coatings show different phase compositions. XRD proves that these coatings before and after thermal cycling have the ideal magnetoplumbite structure. As shown in Fig. 2(a)–(c), the as-sprayed coatings keep the magnetoplumbite structure, and the relatively weak peak intensities indicate that the crystallization is not complete. In the XRD patterns, some peaks could be attributed to those of α,γ-Al_2O_3 and $REAlO_3$ (RE = Nd, Sm, Gd). It is obvious that these MgO-doped RE hexaluminates were partially decomposed during plasma spraying and this process could be expressed as:

$$REMgAl_{11}O_{19} \rightarrow REAlO_3 + MgO + 5Al_2O_3\,(RE = Nd,\ Sm,\ Gd) \quad (1)$$

However, the characteristic peaks of MgO are not clearly observed in the XRD patterns, this may be due to its rather low content in the coatings, which also proves that it has been vaporized by the plasma flame.

Four plasma sprayed coatings were thermally cycled with a gas burner facility. After thermal cycling, the XRD patterns as shown in Fig. 2 indicate that the crystallization is complete, matching well with their corresponding powders and standard JCPDS cards. SrHA coating as shown in Fig. 2(d) has the pure magnetoplumbite structure after thermal cycling and no other phases are formed. It seems that SrHA has a higher phase stabil-

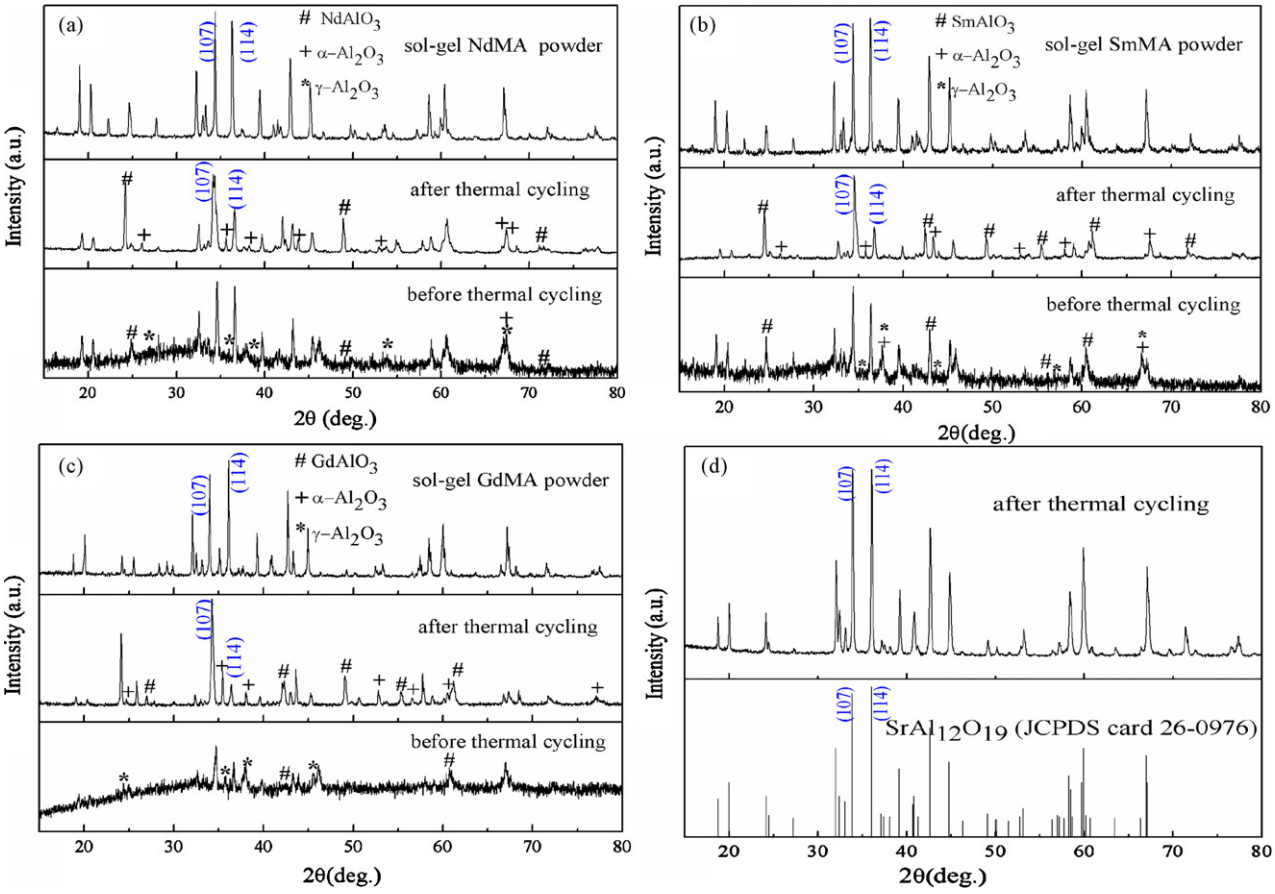

Fig. 2. Comparison of XRD patterns of coatings before and after thermal cycling failure: (a) NdMA, (b) SmMA, (c) GdMA and (d) SrHA.

Table 2
The thermal cycling lifetimes of the four coatings and the radius of large cations with twelve-fold coordination (data after Ref. 32).

Coatings	LaMA	NdMA	SmMA	GdMA	SrHA
Lifetime (cycles)	11,970	5560	2552	2493	1240
Radius of RE^{3+} and Sr^{2+} (pm)	136	127	124	~116	144

ity than the other three oxides in the plasma spraying process. This may be another indirect evidence for the loss of MgO in the RE hexaluminate coatings induced by the vaporization of MgO. On the other hand, for the RE hexaluminate coatings in Fig. 2(a)–(c), the peak of (1 0 7) face is the strongest after thermal cycling, which is different from the LaMA coating[28] and the powders. These observations may prove that the growths of the [1 0 7] and [1 1 4] orientations are dynamically and thermodynamically favored, respectively, due to the anisotropy of their crystal growths.

The thermal cycling lifetimes of these four coatings are listed in Table 2. The NdMA coating has a thermal cycling life of 5560 cycles, nearly half of the LaMA coating, and it is two times longer than those of the SmMA (2552 cycles) and GdMA (2493 cycles) coatings, and four times longer than that of the SrHA (1240 cycles) coating. During thermal cycling, failure occurred by a large area of coating as illustrated in Fig. 3(a)–(d), accounting for much more than 5% of the specimen area, peeling off in one piece instead of the coating spalling bit by bit, and this occurred within the last tens of cycles. The large surface cracks could be clearly observed in SrHA coating after failure as shown in Fig. 3(d). All the coatings seem to have the same failure mode, occurring at the interface between the ceramic top-coat and the bond coat. This can also be proved by the cross-section micrographs of the coatings as shown in Fig. 4(a)–(c). The cracking

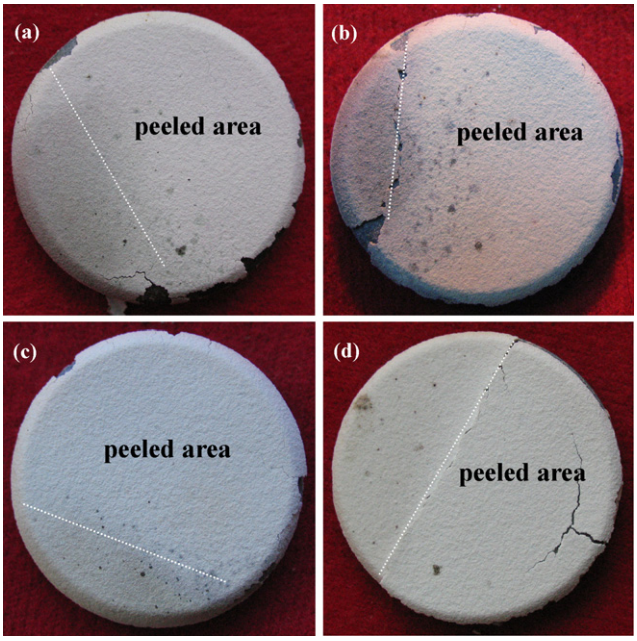

Fig. 3. Surface photos of coatings after thermal cycling failure: (a) NdMA, (b) SmMA, (c) GdMA and (d) SrHA, the white dotted lines are shown as the boundaries for the peeled areas.

formations of these coatings could be probably due to their relative low CTEs ($9.5–9.7 \times 10^{-6}\ K^{-1}$) which are almost the same and independent on the rare earth cations for RE hexaluminates as reported in Bansal's work.[16] In order to study the influence of the TGO growth (mainly the α-Al_2O_3 phase) on the thermal cycling behavior, elemental distributions at the top-coat–bond coat interfaces of NdMA, GdMA and SrHA coatings were determined and their results are shown in Fig. 5(a)–(c), respectively. The large tablets embedded in the aperture of the interfaces are solidified epoxy resins. The formation of TGO is not obvious, which is different from the LaMA coating whose TGO could be clearly observed. This difference may be resulted from the relative short thermal cycling lifetimes of these four coatings compared to that of the LaMA coating and the low oxygen diffusion through the magnetoplumbite oxides.[23] The elemental analysis indicates that TGO has made a rather limited contribution to the failure of these coatings, which is much different from the YSZ coating.

3.2. Comparison of the thermal cycling behaviors of four coatings

Thermal cycling behavior is closely related to the service life of the plasma spayed TBC. Therefore, owing to the thermal cycling lifetime differences of such four coatings cannot be well elucidated by their negligible TGO growths as well as nearly the same CTEs, the inherent crystal chemistry characteristics of such hexaluminate oxides have been taken into consideration in order to better understand the microstructure evolutions and the different thermal cycling lifetimes of these four coatings during thermal cycling.

Compounds with magnetoplumbite structure have the general composition of $A^{2+}B_{12}{}^{3+}O_{19}$. Here, just take the typical compound $SrAl_{12}O_{19}$ as the prototype, and the MgO-doped RE hexaluminates are regarded as its derivatives by ion substitutions. It has a hexagonal structure with the space group of $P6_3/mmc$. As illustrated in Fig. 6(a), each unit cell is composed of two spinel blocks separated by two intermediate mirror planes. The large Sr^{2+} ion is located in the intermediate layer and coordinated by twelve O^{2-} ions (the yellow polyhedron shown in the unit cell). There are five different crystallographic sites in the unit cell for Al^{3+} ions, with the Al(2) trigonal bipyramid site, the Al(3) tetrahedral site, the Al(1), Al(4) and Al(5) octahedral sites. These five different crystallographic sites accommodate the cations substitution with different ion radius. When the large RE^{3+} substitute for Sr^{2+} in the mirror planes and the Mg^{2+} enters the tetrahedral site which is energetically favorable as in $MgAl_2O_4$, the MgO-doped RE hexaluminates ($REMgAl_{11}O_{19}$, RE = La to Gd) could be obtained as shown in Fig. 6(b). The separated mirror planes containing large cations cause effective

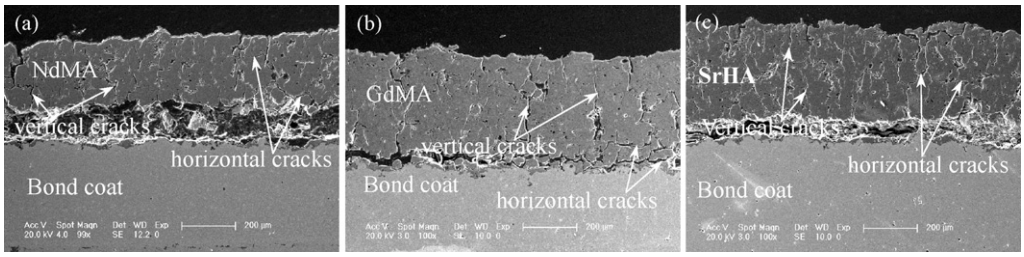

Fig. 4. SEM micrographs of the cross-section of the coatings after thermal cycling failure: (a) NdMA, (b) GdMA and (c) SrHA.

suppression of grain growth along *c*-axis, resulting in the magnetoplumbite oxides whose platelet-like hexagonal crystals have high aspect ratio. The high specific surface areas offer these materials outstanding sintering resistance and widely applications in many other fields.[19–22,30] Experimentally, such materials can hardly reach a relative density above 90% by pressureless-sintered even at 1650 °C.

Surface and fractured cross-section morphologies of the coatings after failure are shown in Figs. 7 and 8, respectively. It is obvious that these coatings have distinct morphology characteristics under the similar thermal cycling test conditions. By comparing the surface micrographs between the as-sprayed and failed coatings as shown in Fig. 1(b) and Fig. 7(a)–(d), respectively, it is interesting to find out that lots of platelet-like hexagonal grains seem to be in situ recrystallized from the molten lamellae of the coatings during thermal cycling. For RE hexaluminate coatings from NdMA to GdMA as illustrated in Fig. 7(a)–(c), the gain size increases, and the sintering of the coating becomes more serious along with the reduction of the RE^{3+} radius, which was also pointed out in Wang's work that the hexaluminate with small RE^{3+} has a high sintering ability.[18] It could be clearly observed in Fig. 7(c), the surface of GdMA coating has been sintered after thermal cycling, and there are a lot of equiaxed grains in its surface which is different from

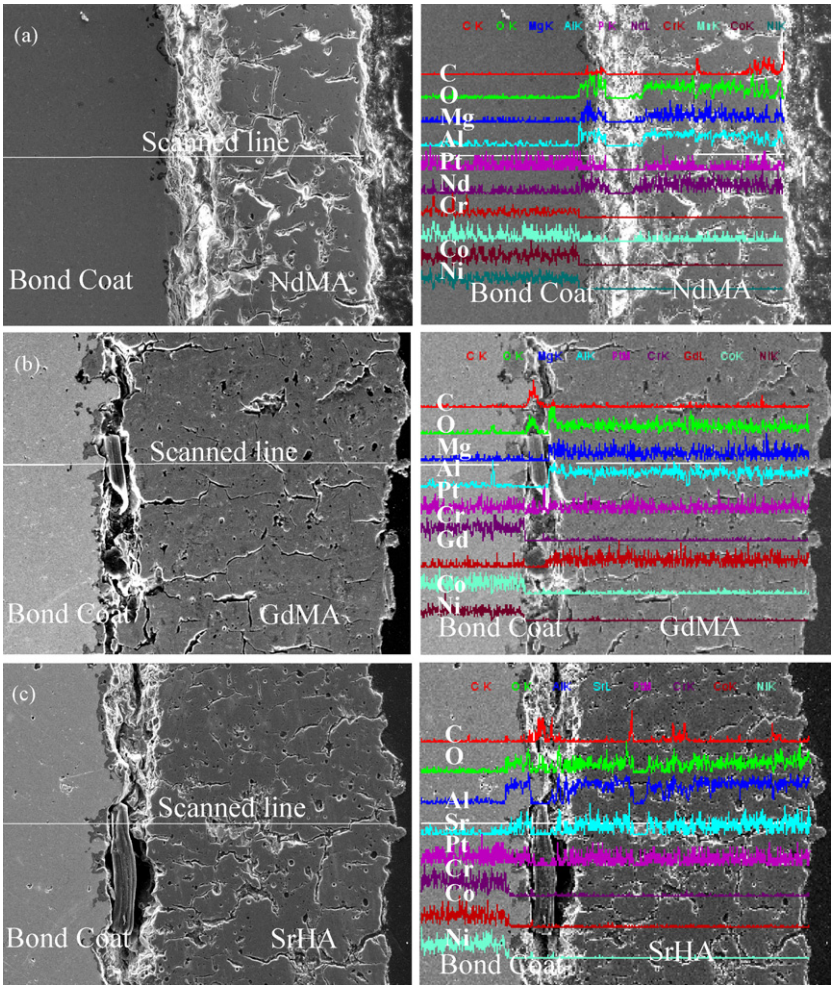

Fig. 5. SEM micrographs of the cross-section (left) and their corresponding line scanning images (right) of the coatings after thermal cycling tests: (a) NdMA, (b) GdMA and (c) SrHA.

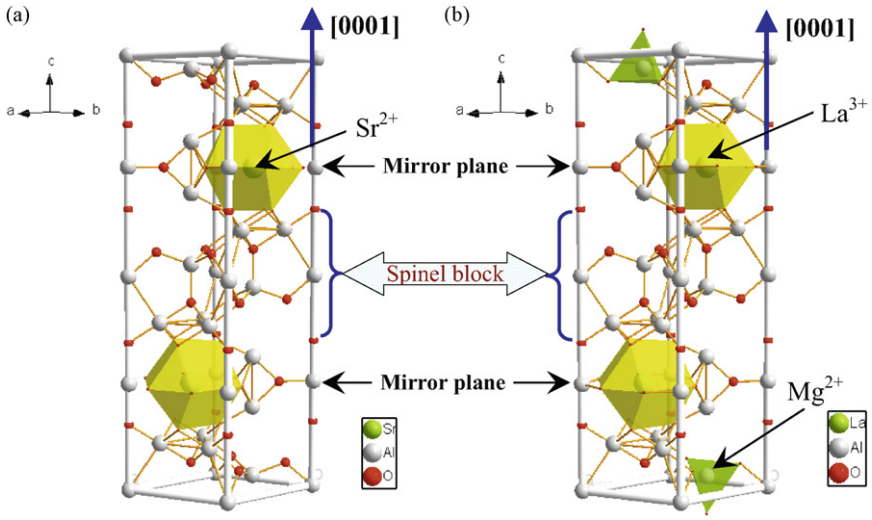

Fig. 6. Crystal structure of (a) $SrAl_{12}O_{19}$ and (b) $LaMgAl_{11}O_{19}$ unite cells with the large cations located in the yellow polyhedron, giving a twelve-fold coordination, Mg^{2+} are located in the green tetrahedron. (For interpretation of the references to color in this figure legend, the reader is referred to the web version of the article.)

other three coatings whose surfaces have the hexagonal grains as illustrated in Fig. 7(a), (b) and (d). The thickness of the platelike hexagonal grains of these four coatings are statistically measured from several randomly selected SEM micrographs of both their surfaces and fractured cross-sections as shown in Figs. 7 and 8, respectively. The grain thickness distributions of these four coatings corresponding to their thermal cycling lifetime and the radius of the large cations in their crystal lattices are illustrated in Fig. 9. After thermal cycling, the average thickness of the large platelet-like hexagonal grains for recrystallized RE hexaluminate coatings including LaMA are in the order: LaMA (70 nm) < NdMA (93 nm) < SmMA (201 nm) < GdMA (217 nm),[28] whereas the average grain thickness of SrHA coating is about 166 nm. By comparing Figs. 7 and 8, it could be observed that the platelet-like hexagonal grains in the coatings' surfaces are larger than those in the coatings' fractured cross-sections. By a more careful analysis, it could be found that GdMA coating surface has larger grains than other coatings. While it is interesting that the grain thickness in fractured cross-sections of GdMA coating is markedly smaller than that of SmMA coating, this may be the reason that SmMA and GdMA coatings have similar average grain thicknesses and similar thermal cycling lifetimes. The morphology differences between the coatings' surfaces and fractured cross-sections are believed to be induced by the different recrystallization rates resulted from the temperature gradient across the coatings' thickness during

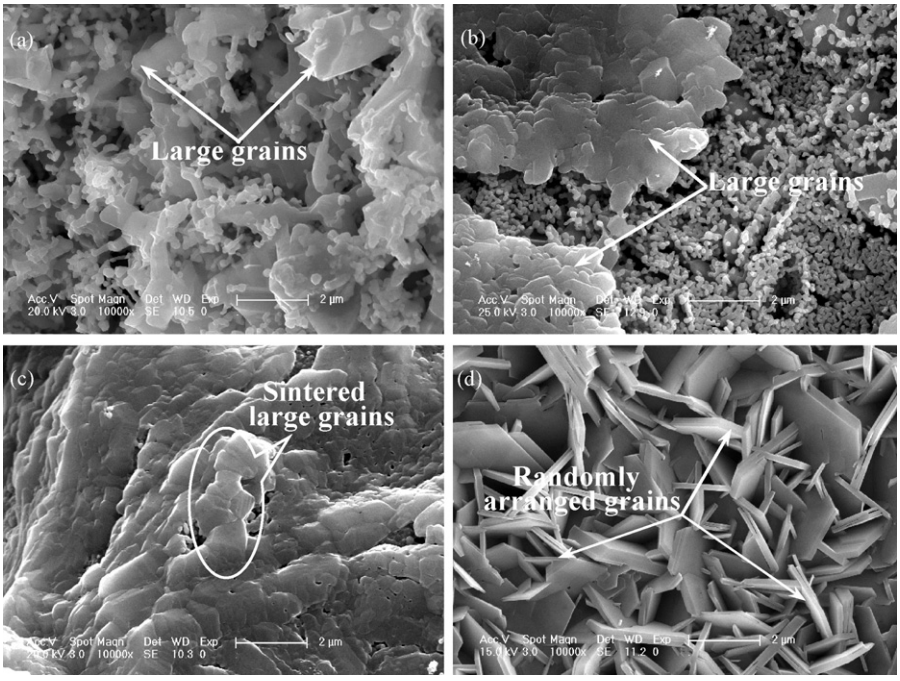

Fig. 7. SEM micrographs of the coatings surfaces after failure with the magnification 10,000×: (a) NdMA, (b) SmMA, (c) GdMA and (d) SrHA.

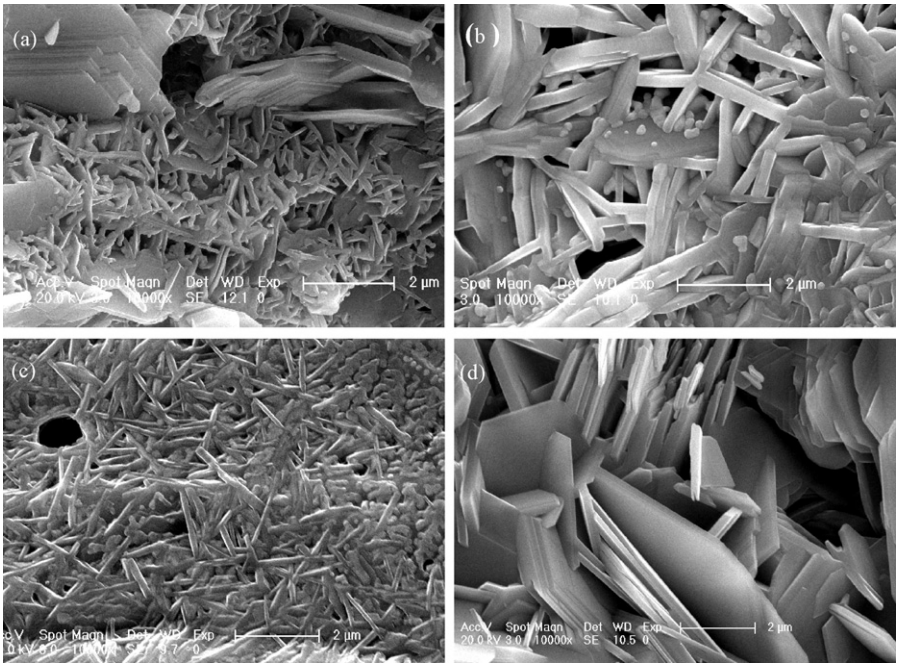

Fig. 8. SEM micrographs of fractured cross-section of the coatings after failure: (a) NdMA, (b) SmMA, (c) GdMA and (d) SrHA.

thermal cycling, and cause large standard deviations to the grain thickness of these four coatings, especially to GdMA as shown in Fig. 9.

Based on the above results, it seems that the radiuses of RE^{3+} ions strongly affect the recrystallization rates of the magnetoplumbite-type RE hexaluminate coatings which finally determine their different thermal cycling lifetimes. Under similar thermal cycling test conditions, the smaller the radius of RE^{3+}, the higher recrystallization rate of the coating and the shorter of the coating's thermal cycling lifetime. Actually, one small thin platelet-like hexagonal grain could be taken as the single crystal of such magnetoplumbite-type oxides. The high aspect ratio of the single crystal is induced by the lowest growth rate of the [0 0 0 1] orientation, whose growth rate is restrained by the separated mirror planes containing large cations as shown in Fig. 6(a) and (b). Hartman and Perdok's PBC (Periodic Bond Chain) theory indicates that the F (flat) face which has the lowest average attachment energy has the lowest growth rate, and determines the final morphology of the crystal growths. The value of the attachment energy could be calculated as the total bond energy of all the chemical bonds among the atoms located in such a face, and the bond energy can be calculated with equation of $E = z_1 z_2 e^2/r$ according to the electrostatic point charge model.[31] As reported in Xu's work the (0 0 0 1) face of LaMA single crystal has the lowest attachment energy and the lowest growth rate leading to the formation of platelet-like hexagonal crystal in the end.[31] Based on this theory, the different attachment energies of their (0 0 0 1) faces for all REMA (RE = La, Nd, Sm, Gd) oxides, which ultimately come down to the different bond energies between the RE^{3+} and O^{2-} ions in the twelvefold coordination polyhedron due to the same of the number and kinds of chemical bonds in combination with the atoms' crystallographic sites of such oxides, may be the inherent factors that determine these coatings' different recrystallization rates and final platelet-like grain thickness after failure. By qualitatively taking the bond energy $E = z_1 z_2 e^2/r$ into consideration, it is not difficult to find out that E for REMA (RE = La, Nd, Sm, Gd) is in the order of $E_{LaMA} < E_{NdMA} < E_{SmMA} < E_{GdMA}$, since the parameters z_1, z_2 and e are constants, the only variable r, the bond length between the RE^{3+} and the O^{2-} ions, is gradually reduced due to lanthanide contraction from La to Gd. The tendency that the cell parameters (both a and c) gradually decrease from LaMA to GdMA has been proved in Kahn's work[19] and our former work.[27] As a result, it could be concluded that the attachment energy of the (0 0 0 1) face gradually increases from LaMA to GdMA due to the change tendency of bond energies, and then the growth rate of (0 0 0 1) face increases with the reduction of RE^{3+} radius, thus the larger the RE^{3+} radius, the thinner the final average grain thickness for such RE hexaluminate coatings after thermal cycling failure as illustrated in Fig. 9.

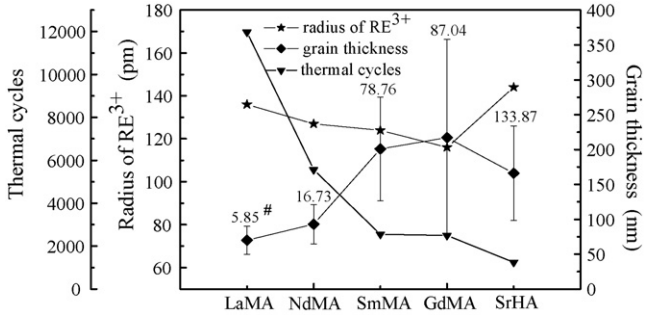

Fig. 9. The thickness of plate-like grains of these four coatings after thermal cycling corresponding to their thermal cycling lifetime (by cycles) and the radius of the RE^{3+} cations, together with LaMA coating from our former work. #*Note*: the number over the symbol ♦ inside the figure is the increase of grain thickness (pm) per thermal cycle.

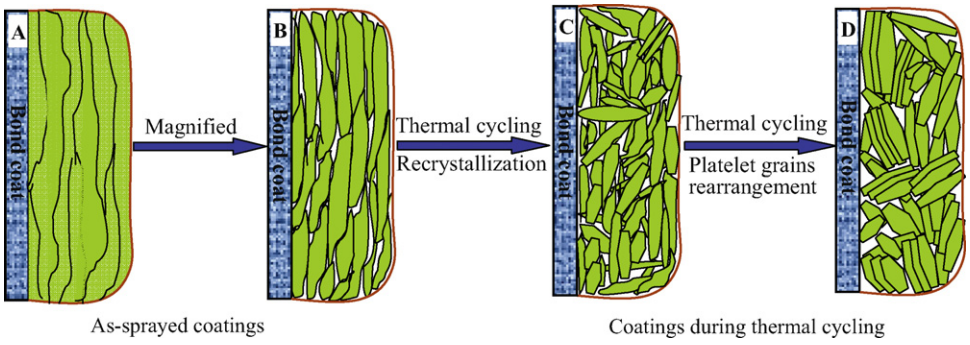

Fig. 10. The typical morphology evolution of plasma-sprayed coatings with magnetoplumbite structure during thermal cycling.

SrHA coating has a high grain growth rate and the shortest thermal cycling lifetime. As illustrated in Fig. 9, the increase of average grain thickness per thermal cycle for these four coatings and LaMA coating is: LaMA (5.85 pm) < NdMA (16.73 pm) < SmMA (78.76 pm) < GdMA (87.04 pm) < SrHA (133.87 pm).[28] The experiment results indicate that a lower bond energy between Sr^{2+} (144 pm) and O^{2-} has not impart a lower grain growth rate of the SrHA coating compared to that of RE hexaluminate coatings during thermal cycling due to the specific crystal chemistry characteristics of SrHA cell such as the kinds of the atoms etc. As discussed above, RE hexaluminates could be taken as the derivatives of the SrHA oxide, the substitutions of RE^{3+} for Sr^{2+} and Mg^{2+} for Al^{3+} in the SrHA unit cell could lead to the formation of $RE^{\bullet}_{Sr}$ and Mg'_{Al} defects,[30] the lattice defect reaction could be expressed as:

$$RE^{\times}_{RE} + Mg^{\times}_{Mg} \rightarrow RE^{\bullet}_{Sr} + Mg'_{Al} \quad (2)$$

Actually, the grain growth of hexaluminates with magnetoplumbite structure are controlled by the diffusion rate of the large cations in the intermediate mirror planes, the radius and valence of the ions, together with the lattice defects would be the important factors to affect their diffusions. Therefore, the lower valence of Sr^{2+} than that of RE^{3+} and the relative less lattice defects in the SrHA lattice would be the main reasons for its fast growth rate of the platelet-like hexagonal grains, and its coating has the shortest thermal cycling lifetime.

The typical morphology evolution of hexaluminate coatings during thermal cycling is illustrated in Fig. 10A–D. The growth and rearrangement of platelet-like hexagonal grains during thermal cycling could offer the coating a larger porosity, resulting in a high strain tolerance, high thermal insulating efficiency and longer thermal cycling lifetime. As shown in Fig. 4(a)–(c), the vertical and horizontal microcracks could be observed in the coatings' cross-sections after failure. The microcrack turning and extending give rise to the release of residual stresses, enhance the coatings' toughness, and then lead to the improvements of the coatings' performance. On the other hand, by a careful analysis of the micrograph as shown in Fig. 4(c), more vertical and horizontal microcracks could be observed in SrHA coating, this may be due to its fast growth rate and more random arrangement of the platelet-like hexagonal grains that contribute to the microcrack turning. In the recrystallization process during thermal cycling, small platelet-like hexagonal grains are firstly formed, and then some of them would rearranged along their (0 0 0 1) faces to reach a lower energy position.[20,33,34] As shown in Fig. 8(a)–(d), some large platelets with a lot of small platelet-like grains located inside could be found in the fractured cross-section micrographs, which also happened for the LaMA coating.[28]

However, the appearance of pores resulted from the platelet-like microstructure of the coating would inevitably reduce the bond strength between the ceramic top-coat and the bond coat, making some contribution to the coatings failure. This may be another mortal factor leading to the failure of the hexaluminate coatings except the CTE mismatch between the ceramic coating and the bond coat. Moreover, this effect would be more prominent with the increase of gain growth rates resulting from recrystallization, and this may be the main factor that determines the much different thermal cycling lifetimes of these four coatings.

4. Conclusions

MgO-doped RE hexaluminate coatings $REMgAl_{11}O_{19}$ (RE = Nd, Sm, Gd) with magnetoplumbite structure have longer thermal cycling lifetimes than SrHA. During thermal cycling, the in situ recrystallization and rearrangement of platelet-like hexagonal grains from the molten lamellae of the coatings lead to the formation of a large porosity, low thermal conductivity, high strain tolerance, high sintering resistance of these hexaluminate coatings and accordingly result in good thermal cycling properties. No obvious TGO formation was observed in these coatings after thermal cycling. Apart from the factors such as their relatively low CTEs compared with that of bond coat, the recrystallization and sintering of the as-sprayed coatings during thermal cycling would weaken the bond strength of the coating, and these may be very important factors for coatings failure.

The thermal cycling lifetime differences of these coatings seem to be strongly dependent on the gain growth during thermal cycling. For the RE hexaluminate coatings, the larger the radius of RE^{3+}, the lower the grain growth rate and the longer the thermal cycling lifetime. SrHA coating has an inferior thermal cycling lifetime to the RE hexaluminate coatings, and this may be induced by the faster growth of the platelet-like hexagonal grains than that of the RE hexaluminates.

Acknowledgements

Many thanks to Dr. Q. S. Wang of Beijing Polytechnic University for the assistance in plasma spraying, Ms. M. Y. Li for the SEM and EDS measurement. Financial supports from projects NSFC-50825204, NSFC-20921002 and Hunan Provincial Key Laboratory of Materials Protection for Electric Power and Transportation (Changsha University of Science & Technology) are also gratefully acknowledged.

References

1. Padture NP, Gell M, Jordan EH. Thermal barrier coatings for gas-turbine engine applications. *Science* 2002;**296**(4):280–4.
2. Miller RA. Current status of thermal barrier coatings—an overview. *Surf Coat Technol* 1987;**30**:1–11.
3. Cao XQ. Application of rare earths in thermal barrier coating materials. *J Mater Sci Technol* 2007;**23**(1):15–35.
4. Clarke DR, Phillpot SR. Thermal barrier coating materials. *Mater Today* 2005;**8**(6):22–9.
5. Schulz U, Peters M, Bach Fr-W, Tegeder G. Graded coatings for thermal, wear and corrosion barriers. *Mater Sci Eng A* 2003;**362**(1–2):61–80.
6. Cao XQ, Vassen R, Stoever D. Ceramic materials for thermal barrier coatings. *J Eur Ceram Soc* 2004;**24**(1):1–10.
7. Clarke DR, Levi CG. Materials design for the next generation thermal barrier coatings. *Annu Rev Mater Res* 2003;**33**:383–417.
8. Clarke DR. Materials selection guidelines for low thermal conductivity barrier coatings. *Surf Coat Technol* 2003;**163–164**:67–74.
9. Gleeson B. Thermal barrier coatings for aeroengine applications. *J Propulsion Power* 2006;**22**(2):375–83.
10. Ma W, Mack DE, Vassen R. Perovskite-type strontium zirconate as a new material for thermal barrier coatings. *J Am Ceram Soc* 2008;**91**(8):2630–5.
11. Vassen R, Cao XQ, Tietz F, Basu D, Stöver D. Zirconates as new materials for thermal barrier coatings. *J Am Ceram Soc* 2000;**83**(8):2023–8.
12. Vassen R, Cao XQ, Tietz F, Kerkhoff G, Stoever D. $La_2Zr_2O_7$—a new candidate for thermal barrier coatings. In: Lugscheider E, Kammer PA, editors. *Proceedings of the United Thermal Spray Conference '99*. Duesseldorf, Germany: ASM Thermal Spray Society; 1999. p. 830–4.
13. Lehmann H, Pitzer D, Pracht G, Vassen R, Stoever D. Thermal conductivity and thermal expansion coefficients of the lanthanum rare-earth-element zirconate system. *J Am Ceram Soc* 2003;**86**(8):1338–44.
14. Cao XQ, Vassen R, Tietz F, Stoever D. Lanthanum-cerium oxide as a thermal barrier-coating material for high-temperature applications. *Adv Mater* 2003;**15**(17):1438–42.
15. Dai H, Zhong XH, Li JY, Meng J, Cao XQ. Neodymium–cerium oxide as new thermal barrier coating material. *Surf Coat Technol* 2006;**201**(6):2527–33.
16. Bansal NP, Zhu DM. Thermal properties of oxides with magnetoplumbite structure for advanced thermal barrier coatings. *Surf Coat Technol* 2008;**202**(12):2698–703.
17. Choi SR, Bansal NP, Zhu DM. Mechanical and thermal properties of advanced oxide materials for higher-temperature coatings applications. *Ceram Eng Sci Proc* 2005;**26**(3):11–9.
18. Wang XH, Lejus AM, Vivien D, Collongues R. Synthesis and characterization of lanthanide aluminum oxynitrides with magnetoplumbite like structure. *Mater Res Bull* 1988;**23**(1):43–9.
19. Kahn A, Lejus AM, Madsac M, Thery J, Vivien D. Preparation, structure, optical, and magnetic properties of lanthanide aluminate single crystals ($LnMAl_{11}O_{19}$). *J Appl Phys* 1981;**52**(11):6864–9.
20. Mallamaci MP, Sartain KB, Carter CB. Crystallization of calcium hexaluminate on basal alumina. *Philos Mag A* 1998;**77**(3):561–75.
21. Xie L, Cormack AN. Cation distribution in magnetoplumbite and β″-alumina structures. *Mater Lett* 1990;**9**(11):474–9.
22. Sánchez-Herencia AJ, Moreno R, Baudín C. Fracture behaviour of alumina-calcium hexaluminate composites obtained by colloidal processing. *J Eur Ceram Soc* 2000;**20**(14):2575–83.
23. Schaefer GW, Gadow R. Lanthanum aluminate thermal barrier coating. *Ceram Eng Sci Proc* 1999;**20**(4):291–7.
24. Friedrich C, Gadow R, Schimer T. Lanthanum hexaaluminate—a new material for atmospheric plasma spraying of advanced thermal barrier coatings. *J Therm Spray Technol* 2001;**10**(4):592–8.
25. Friedrich C, Gadow R, Lischka MH. Lanthanum hexaaluminate thermal barrier coatings. *Ceram Eng Sci Proc* 2001;**22**(4):375–82.
26. Gadow R, Lischka M. Lanthanum hexaaluminate-novel thermal barrier coatings for gas turbine applications-materials and process development. *Surf Coat Technol* 2002;**151/152**:392–9.
27. Zhang JF, Zhong XH, Cheng YL, Wang Y, Xu ZH, Chen XL, et al. Thermal-shock resistance of $LnMgAl_{11}O_{19}$ (Ln = La, Nd, Sm, Gd) with magnetoplumbite structure. *J Alloys Compd* 2009;**482**(1–2):376–81.
28. Cao XQ, Zhang YF, Zhang JF, Zhong XH, Wang Y, Ma HM, et al. Failure of the plasma-sprayed coating of lanthanum hexaluminate. *J Eur Ceram Soc* 2008;**28**(10):1979–86.
29. Saruhan-Brings B, Schulz U, Kroder CJ. Thermal-insulating material having an essentially magnetoplumbitic crystal structure. Patent no. US 2006/0019107; 2006.
30. Park JG, Cormack AN. Crystal defect chemistry of strontium hexaaluminate magnetoplumbite. *Korean J Crystallogr* 2000;**11**(3):176–81.
31. Xu J, Ma XS, Zhang XM, Shen YF, Wu GZ. The relation between structure and morphology of magnetoplumbite-type crystal $LaMgAl_{11}O_{19}$. *Cryst Res Technol* 1993;**28**(3):365–9.
32. Shannon RD. Revised effective ionic radii and systematic studies of interatomic distances in halides and chalcogenides. *Acta Cryst* 1976;**A32**:751–67.
33. Song JH, Jo YJ, Bang HG, Park SY. Abnormal grain growth mechanism of calcium hexaluminate phase. *Mater Sci Forum* 2007;**534–536**:485–8.
34. Park SY, Song JH, Cho YJ. Effect of grain orientation on the abnormal grain growth with magnetoplumbite crystal structure. *Mater Sci Forum* 2007;**558–559**:1265–70.